



pubs.acs.org/cm

Understanding the Formation Mechanism of Magnetic Mesocrystals with (Cryo-)Electron Microscopy

Giulia Mirabello,^{†,‡} Arthur Keizer,^{†,||} Paul H. H. Bomans,^{†,‡} András Kovács,[§] Rafal E. Dunin-Borkowski,[§] Nico A. J. M. Sommerdijk,*,^{†,‡} and Heiner Friedrich*,^{†,‡}

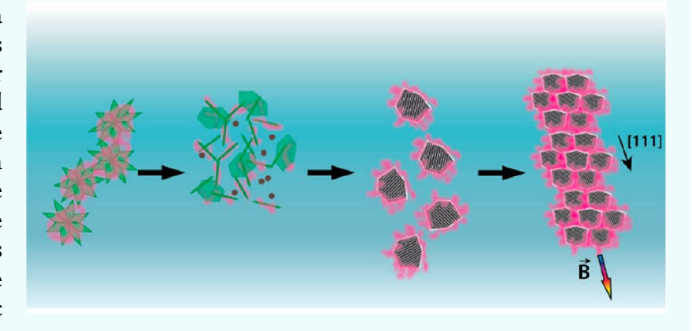
[†]Laboratory of Materials and Interface Chemistry and Center for Multiscale Electron Microscopy, Department of Chemical Engineering and Chemistry, Eindhoven University of Technology, Het Kranenveld 14, P.O. Box 513, 5600 MB Eindhoven, The Netherlands

*Institute for Complex Molecular Systems, Eindhoven University of Technology, P.O. Box 513, 5600 MB Eindhoven, The Netherlands

§Ernst Ruska-Centre for Microscopy and Spectroscopy with Electrons and Peter Grünberg Institute, Forschungszentrum Jülich, 52428 Jülich, Germany

Supporting Information

ABSTRACT: Magnetite (Fe₃O₄) nanoaggregates with a flower-like morphology are considered promising materials in the field of magnetically induced hyperthermia in cancer therapy due to their good heating efficiency at low applied alternating magnetic fields. Although the structure and the magnetic state of such flower-like aggregates have been investigated previously, the mechanism that leads to the hierarchical morphology is still poorly understood. Here, we study the formation mechanism of Fe₃O₄ aggregates synthesized through the partial oxidation of ferrous hydroxide in the presence of poly(acrylic acid) by using cryogenic electron microscopy. The aggregates are formed through a



multistep process involving first the conversion of ferrous hydroxide precursors in ~5 nm primary particles that aggregate into ~10 nm primary Fe₃O₄ crystals that finally arrange into the secondary mesocrystal structure. High-resolution electron tomography is used to show that the Fe₃O₄ mesocrystals are composed of ~10 nm subunits, often showing a uniform crystallographic orientation resulting in single-crystal-like diffraction patterns. Furthermore, electron holography reveals that mesocrystals have a single magnetic domain despite polymeric interfaces between subunits being present throughout the mesocrystal. Our findings could be used to design materials with specific properties by modulating the morphology and/or magnetic state that is suitable for biomedical application.

■ INTRODUCTION

The use of specifically designed nanoparticles (NPs) for cancer diagnosis and treatment has recently attracted more attention. 1-3 In particular, magnetite (Fe₃O₄) is considered to be one of the most promising materials as it possesses a high saturation magnetization. Moreover, due to its biocompatibility, magnetite is a contrast agent in magnetic resonance imaging (MRI) and can be used in targeted drug delivery systems.4,5

The magnetic properties of Fe₃O₄-NPs have been exploited to locally induce cell necrosis in magnetically mediated hyperthermia for cancer therapy. $^{6-8}$ When an external alternating magnetic field is applied, the magnetic domains convert magnetic energy into heat, due to loss of hysteresis, Néel relaxation, or induced Eddy currents.^{3,9} The temperature can be locally increased above 42 °C, which is known to interfere with many cell functions (cell growth and differentiation), which, in turn, leads to apoptosis. 10,11

Although the Fe₃O₄-NPs has been successfully employed in in vivo hyperthermia therapy for small animals, 12,13 clinical human studies have been very limited. 14-16 The problems of accurate thermometry within the tumor mass, precise tumor heating, preventing damage of the surrounding healthy tissues, and the accumulation of intravenously administrated Fe₃O₄-NPs in healthy tissues, such as liver and kidneys, make the treatment still very challenging.¹⁷ Therefore, recent studies have been focused on optimizing the heating efficiency of the Fe₃O₄-NPs. 18,19 The heating efficiency is measured in terms of the specific absorption rate (SAR), which in turns depends on the magnetic saturation (M_s) and the volume ratio of the Fe₃O₄-NPs. ^{20,21} Magnetite clusters embedded in polymers with a flower-like morphology are the most investigated system

Received: May 9, 2019 Revised: August 1, 2019 Published: August 12, 2019



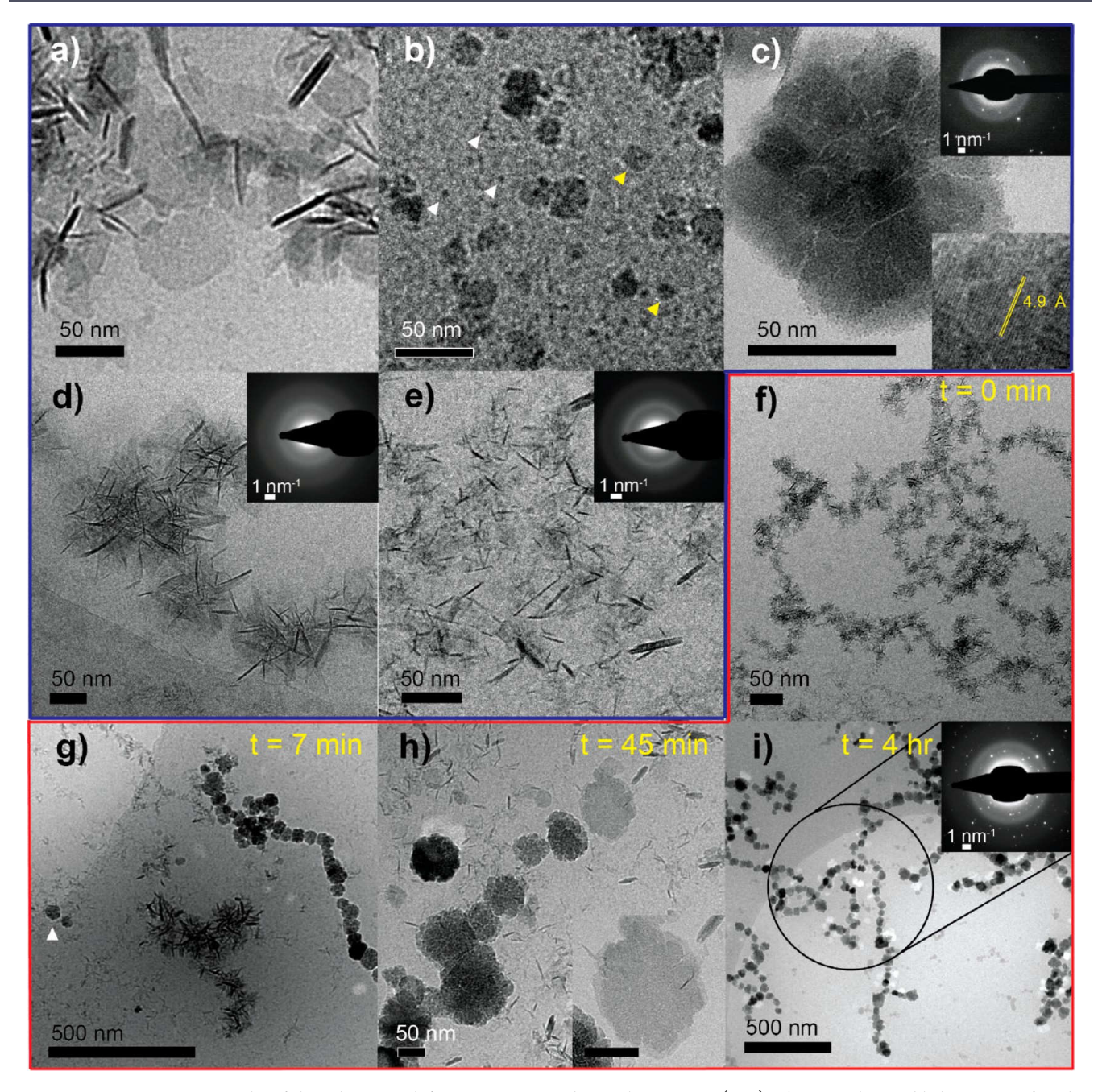


Figure 1. Cryo-TEM micrographs of the solution at different time points during the reaction. (a—e) Objects and assembled structures found in solution (blue border): (a) green rust platelets, (b) primary particles (white arrows) and primary magnetite crystals (yellow arrows), (c) flower-like magnetite aggregates, (d) star-like green rust aggregates, and (e) green rust platelet network. (f—i) Time series showing the morphological progression during magnetite synthesis (red border): (f) solution at 0 min, showing star-like green rust aggregates arranged in strings, (g) solution at 7 min showing magnetite aggregates arranged in strings together with green rust aggregates (the arrow highlights individual dispersed magnetite aggregates), (h) solution at 45 min, showing the dissolution of the green rust to form magnetite (the inset shows an enlargement of a dissolving green rust platelet), and (i) magnetite aggregate strings. The insets in panels c—f and i are the SAED patterns of the areas shown in the corresponding images. The assignment of reflections for the SAED pattern shown in panel c can be found in Supporting Information section 1 and Figure S1.

for magnetically mediated hyperthermia, as they have shown a high SAR at low applied alternating magnetic fields. ^{18,22,23}

Magnetite nanoclusters can be synthesized at high temperatures (>90 °C) by polyol methods. ^{18,23-27} Depending on the specific polymer that is used during synthesis, the crystal size can vary over a wide range (35–200 nm). The resulting magnetite crystals consist of smaller subdomains arranged into a flower-like morphology that are often crystallographically

aligned. Such a polydomain crystal showing a single crystal-like diffraction pattern is termed a mesocrystal. $^{28-30}$ Although the structure and the magnetic properties have been well investigated in terms of hyperthermia performance, very little is known about the formation mechanism that leads to such hierarchical crystals. It has been proposed that the superstructure obtained via aqueous polyol synthesis is formed starting from the agglomeration of ferrihydrite-like $\sim\!\!2$ nm

primary particles formed in the presence of Fe^{2+, 2.5} with a mechanism similar to what was reported in 2013 for the coprecipitation of Fe²⁺ and Fe³⁺ at room temperature in the absence of additives.³¹ However, there are no *in situ* observations of the formation mechanism that can confirm this hypothesis. In fact, most studies have been focused on the characterization of the final product with *ex situ* techniques. Furthermore, intermediate stages during the formation of magnetite nanoflowers have been investigated with only conventional (dry) transmission electron microscopy (TEM),²⁵ which often introduces artifacts caused by the drying process or by the exposure to oxygen.³² In contrast, cryogenic TEM (cryo-TEM) can image the solution in its native hydrated state, giving the great advantage of avoiding the formation of these artifacts.³³

In this study, we present a time-resolved analysis of the different stages during the formation of flower-like magnetite crystals using cryo-TEM. The magnetite crystals were synthesized using the partial oxidation method in the presence of poly(acrylic acid) (pAA). This is a well-known aqueous synthetic method, involving a ferrous hydroxide precursor. 34,35 pAA was chosen as an additive because of its well-known affinity for the iron oxide surface, biocompatibility, and water solubility. Furthermore, we have performed high-resolution electron tomography (HR-ET) to resolve the hierarchical three-dimensional (3D) structure and off-axis electron holography (EH) to study the magnetism of the crystals. The results show that magnetite mesocrystals are formed through a multistep process, involving $Fe(OH)_2$ as a precursor and different intermediate structures. Unraveling the formation steps of this hierarchical structure is important in the manipulation of the aggregation steps. We believe that a better understanding of the formation mechanism of this magnetic superstructure will aid the future design of materials with tunable properties for biomedical applications, such as therapeutic agents in cancer treatment.

■ RESULTS AND DISCUSSION

Magnetite nanocrystals were synthesized in water through the partial oxidation of ferrous hydroxide in the presence of pAA as reported by Altan at al.²⁷ In short, an aqueous solution containing KOH (0.14 M), KNO₃ (0.2 M), and pAA (450 kDa, \sim 4 × 10⁻⁶ M) was degassed with nitrogen gas for approximately 30 min, and then the mixture was added to an FeSO₄ solution (0.026 M). The overall synthesis was performed under a nitrogen flow at 90 °C for ~4 h. A detailed synthesis protocol of Fe₃O₄-pAA can be found in Materials and Methods. Immediately after the addition of the KOH/KNO₃/ pAA mixture to the FeSO₄ solution the iron precipitates as green rust,³⁶ consisting of partially oxidized ferrous hydroxide. Subsequently, magnetite is formed by the oxidation of the green rust, via a dissolution-reprecipitation process.³⁵ Thus, green rust can be considered as both a precursor phase and a reserve of iron ions that have an inherent low solubility in water. Beyond the reaction conditions used in this work, it is well-known that additional factors,³⁷ such as the concentration of the Fe, base, and oxidant, can influence the final Fe₃O₄ crystal size and morphology, for which we would like to refer to the work of Vereda et al.³⁸

We investigated the evolution of morphology and crystallinity during magnetite formation using cryo-TEM in combination with low-dose selected-area electron diffraction (SAED) (Figure 1 and Supporting Information section 1). For

this, samples were prepared at different time points during the reaction by plunge freeze vitrification. Time zero is taken as the moment immediately after mixing of the reagents.

The cryo-TEM micrographs taken at the different times show the presence of different objects in solution (Figure 1ae): green rust platelets (Figure 1a), primary particles (white arrows in Figure 1b), primary magnetite crystals (yellow arrows in Figure 1b), and secondary magnetite aggregates with a flower-like morphology (Figure 1c and Figure S1). At alkaline pH, the surface of the green rust is positively charged while the magnetite surface negative. 39,40 Because pAA is a negatively charged polyelectrolyte under these conditions, it will adsorb on the green rust surface, while an electrostatic repulsion is expected to act between pAA and the magnetite surface. However, electrostatic repulsions do not occur as the carboxylate groups are known to coordinate with the Fe atoms on the surface, 41 as demonstrated in nature for the C-termini of proteins involved in the biomineralization of magnetite in $magnetotactic\ bacteria.^{42}$

At t_0 (time zero), the solution is composed of only thin hexagonal platelets consistent with other reports about green rust type 2 (Figure 1f and Figure S2; see Supporting Information section 2 for details).⁴³

A majority of these green rust platelets are organized in dense star-like aggregates (Figure 1d) that in turn are arranged in strings (Figure 1f). However, as the reaction proceeds, the frequency of dense star-like aggregates decreases while the frequency of open networks of precursor platelets increases (Figure 1e). The formation of these star-like green rust aggregates could be due to the bridging flocculation phenomenon⁴⁴ driven by the adsorption of pAA onto the green rust precursor surface (Supporting Information section 3). While magnetite is formed, the green rust crystals are consumed as observed via cryo-TEM where their shape starts to deviate from the ideal hexagon (inset in Figure 1h and Figure S3c). At the end of the reaction, the solution contains only magnetite crystal aggregates, indicating that all of the green rust is completely converted (Figure 1i and Figure S1). At 7 min, magnetite crystals with a flower-like morphology as previously reported have already formed.^{26,27} The Fe₃O₄ crystals are present either as individual crystals or in chains (Figure 1g and Figures S3 and S4) and have an average size of 52 ± 12 nm, in good agreement with what was previously reported.²⁷ Surprisingly, a majority of the magnetite crystals always appear to have a crystal size within the range of the calculated average size regardless of the reaction time (see Supporting Information section 4 and Figure S5), while their frequency increased with time. The fact that the crystal size is roughly constant will depend on various factors, such as the formation rate and adsorption of the polymer on the magnetite surface. The SAED pattern of one aggregate shows a singlecrystal diffraction pattern (inset in Figure 1c and Figures S1 and S4) indicating the crystallographic alignment of the subunits. Such mesocrystalline structure was previously observed for similar magnetite aggregates synthesized in the presence of pAA, diethylene glycol, and polyarginine. 18,26,45 Electron diffraction has confirmed the single-crystalline structure of the Fe₃O₄ but fails to provide information about the 3D crystallographic organization.

Hence, to fully understand the hierarchical structure of these aggregates and to determine whether the subunits are crystallographically aligned into a mesocrystalline structure, we need to investigate the 3D morphological and crystallo-

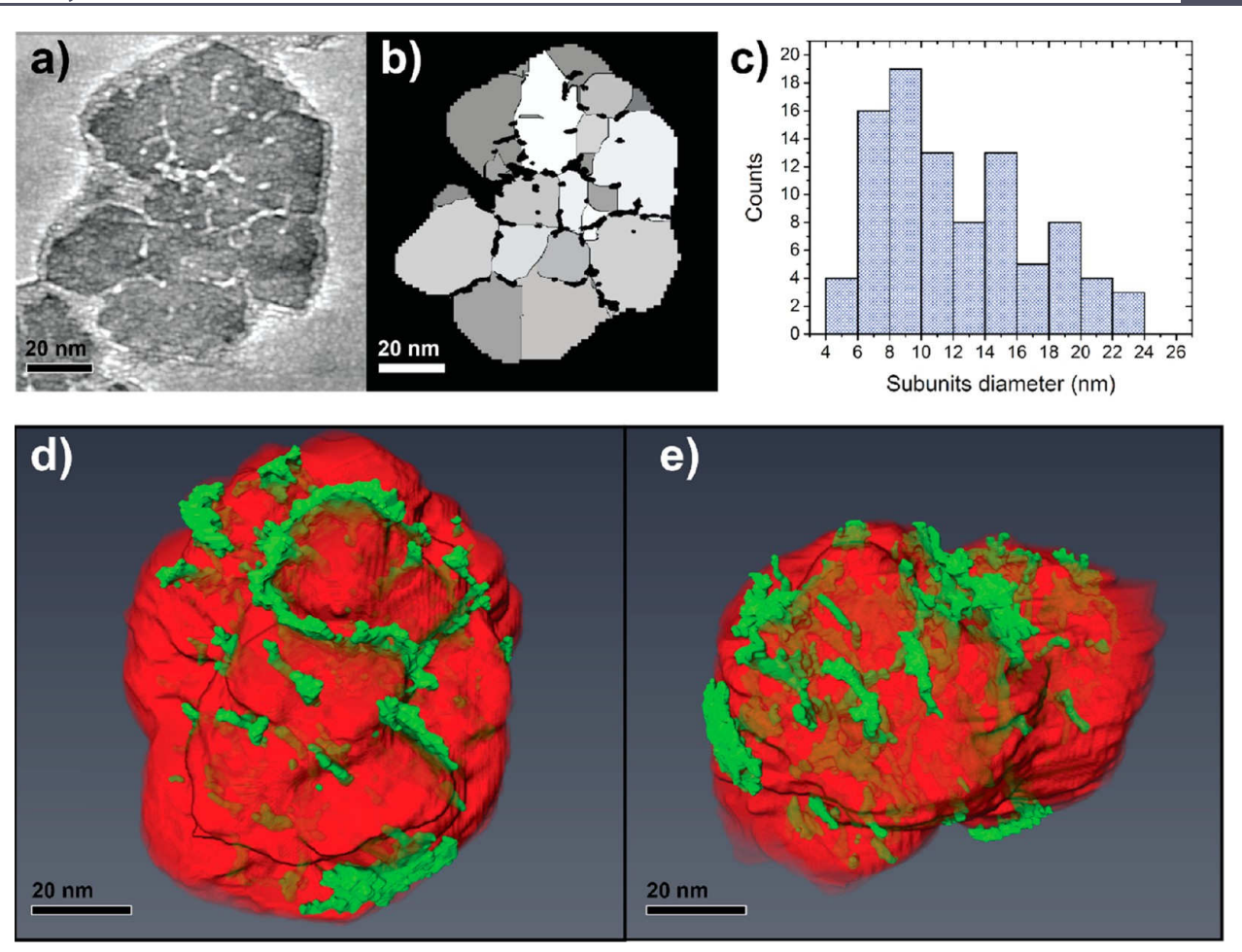


Figure 2. Electron tomogram of the magnetite aggregate. (a) Numerical cross section through reconstruction. (b) Magnetite aggregate segmented into subdomains. Each different shade of gray represents an individual subdomain. (c) Diameter distribution of the identified subdomains after processing. (d and e) Computer volume visualization of the reconstructed tomogram of a single magnetite aggregate. In green are highlighted the gaps between the magnetite subunits, which are colored red.

graphic organization of the aggregates. For this, we performed electron tomography (Figure 2; see Materials and Methods and Supporting Information section 5) by acquiring a series of high-resolution images at different tilt angles (tomographic tilt series). The point resolution is defined as the first zero of the contrast transfer function (CTF).46 For our acquisition conditions (0.095 nm/pixel and -300 nm defocus), it is 0.8 nm, while the information limit is ~1.5 Å (Supporting Information section 5.1). Thus, some images of the acquired tomographic tilt series contain lattice information allowing us to detect the common d spacings for magnetite. To study the orientation of the subunits, the tomographic tilted series was aligned, filtered to point resolution, and reconstructed (Supporting Information section 5.2). The reconstructed tomogram (Figure 2a and Video S1) shows that the structure is composed of subunits and low-density areas (or gaps) that penetrate through the entire volume of the crystal, confirming the cryo-TEM observations. Also, these gaps between the subunits were not uniformly distributed in the structure but with subunits that appear to have partially coalesced. Because the carboxylic acid groups of pAA are known to strongly interact with the Fe ions on the surface of Fe₃O₄, ²⁷ these gaps contain most probably the polymer that was adsorbed on subunits during the formation process, in agreement with what

was previously observed by elemental analysis of magnetite mesocrystals formed in the presence of polyarginine.⁴⁵

To resolve the complexity of the structure and the distribution of the gaps, we have processed the reconstructed tomogram using a multistep algorithm (Videos S2 and S3, and see Supporting Information section 5.3 for more details) to obtain a volume segmentation of the aggregate subunits (Figure 2b,c and Video S4). The processing provides extra information about the shape, the organization of the subunits, and a quantitative estimation of the size range of the subunits. It should be noted that the volume segmentation of the subunits was performed on a cropped volume of the reconstructed tomogram containing a single aggregate to reduce the amount of data to be processed. From the results of the volume segmentation, we determined the diameter range by considering a sphere of equivalent volume representing the segmented subunits. The obtained average diameter of a subunit is 12.1 ± 4.7 nm (Figure 2c), which is twice the size of the smallest feature observed via cryo-TEM (Figure 1b). Therefore, flower-like magnetite crystal aggregates must be formed through a multiple-assembly process. The precursor converts into primary particles that aggregate to form the subunits, which in turn assemble into the flower-like morphology. However, Fe₃O₄ crystal growth promoted by local Fe supersaturation, due to dissolution-reprecipitation of

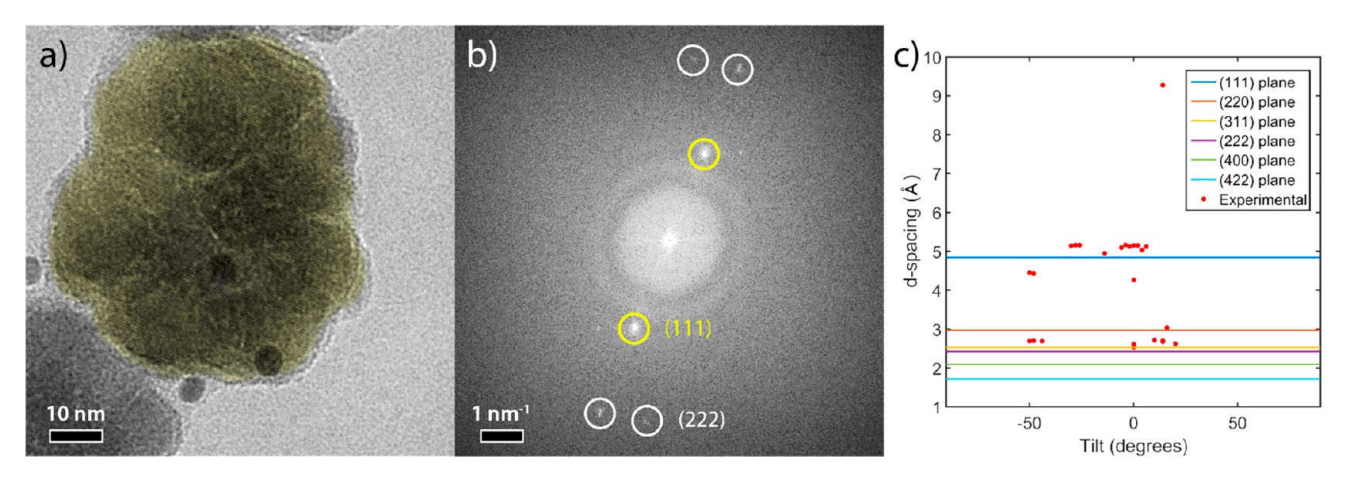


Figure 3. (a) Single electron micrograph extracted from the tomographic tilt series of a typical magnetite aggregate. (b) FFT of panel a showing diffraction reflections consistent with the magnetite mineral phase. The noncircled spots correspond to \sim 4 Å, not consistent with magnetite, and might be due to the gold nanoparticles used for labeling of the tomogram. The yellow area in panel a shows the Fourier filtering analysis. (c) Graph of the d spacings as a function of the tilt angle. The lines indicate the reference d spacings for the magnetite mineral phase, while the dots represent the experimental d spacings obtained from the FFT of the tomographic tilt series.

the green rust platelets and concomitant inclusion of pAA, cannot be excluded. Nevertheless, such a growth mechanism would imply the presence of green rust in the proximity of the growing Fe_3O_4 crystal, which is not frequently observed in the TEM images. A majority of the subunits have a crystal size below the superparamagnetic (SP) regime (<20 nm); however, a few are on the edge of the magnetically stable single-domain (SSD) regime (\sim 25 nm).

The 3D reconstructed volume visualization (Figure 2d,e) shows how the gaps (in green) are distributed in the magnetite aggregate through the subunits (in red). Interestingly, the volume visualization further shows that the gaps are placed at approximately 90° to each other, suggesting a preferential absorption of the polymer onto the surface crystal aggregate.

The crystallographic orientation of the subdomains was investigated by a different analysis approach using again the data of the tomographic tilt series (Figure 3 and Supporting Information section 5.4). First, a Ffast Fourier transform (FFT) of each image of the tomographic tilt series was calculated, which contains lattice information in the form of diffraction spots (Figure 3b). From these spots, the lattice plane d spacing can be measured. This analysis gives access to the 3D crystallographic orientation of the subdomains. We performed Fourier filtering on the FFT images to enhance the area of the aggregates that have generated the diffraction spot, a process we term backmapping (Figure 3a; see Supporting Information section 5.4 for more details). The superimposed image of the Fourier filtering with the original TEM micrograph shows the good level of alignment of the subunits. The degree of alignment of the subunits can be estimated from the colored area representing the region of the aggregates that have generated the *d* spacing in the FFT.

All of the d spacings determined from the FFT tilt series can be plotted as a function of the rotation angle (Figure 3c), showing the observed crystalline planes. The d spacings are consistent with magnetite; however, they are all slightly larger than the reference X-ray diffraction d spacings due to the different calibration method. Furthermore, the few reflections at a d spacing of 4.2 Å might be assigned as the (200) crystalline plane of magnetite. The results of morphological and crystallographic analysis of the tomography demonstrate that these magnetite aggregates are composed of \sim 10 nm

subunits that are crystallographically aligned in the same directions. However, a small percentage of the subunits (<1%) exhibit only one-dimensional alignment along the (111) direction. Although some of the subunits coalesced, we conclude that the aggregates consist of crystallographically aligned subunits, thus having the main characteristic of a mesocrystalline structure.

To investigate the magnetic properties of individual Fe_3O_4 mesocrystals, we used off-axis electron holography (EH) in a transmission electron microscope (Figure 4). EH measures

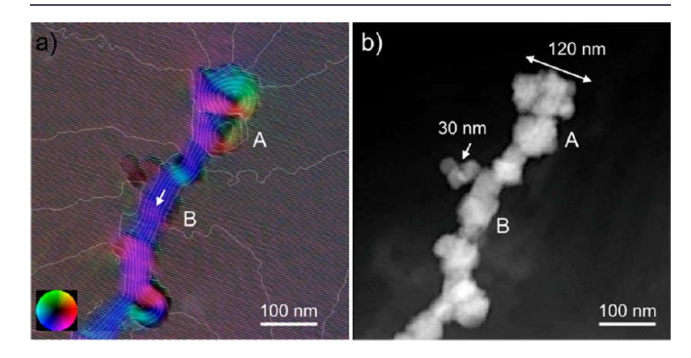


Figure 4. Off-axis electron holography analysis of a chain of $\rm Fe_3O_4$ mesocrystals containing crystals of variable size from 30 to 120 nm. (a) Magnetic phase contours (0.2 rad spacing) formed from the inplane magnetic field contribution to the phase shift overlapped with the electron hologram of the mesocrystals. The magnetic induction is indicated using an arrow and according to the color wheel shown. The two last crystals on the upper side of the chain show a complex magnetic state. (b) MIP of the mesocrystal chain shows the inhomogeneity of the intensity distribution within the crystals.

the phase shift of the electrons that interact with the magnetic field and the electrostatic potential of the sample with a spatial resolution close to 8 nm (see Materials and Methods and Supporting Information section 6 for details).

The phase shifts related to the magnetic flux density (Figure 4a) and the mean inner potential (MIP) (Figure 4b) are separated from the total phases retrieved from a pair of holograms, in which the magnetite chain is magnetically saturated in opposite directions. The studied chain contains crystals of different sizes, from ~30 nm, the smallest, to 120

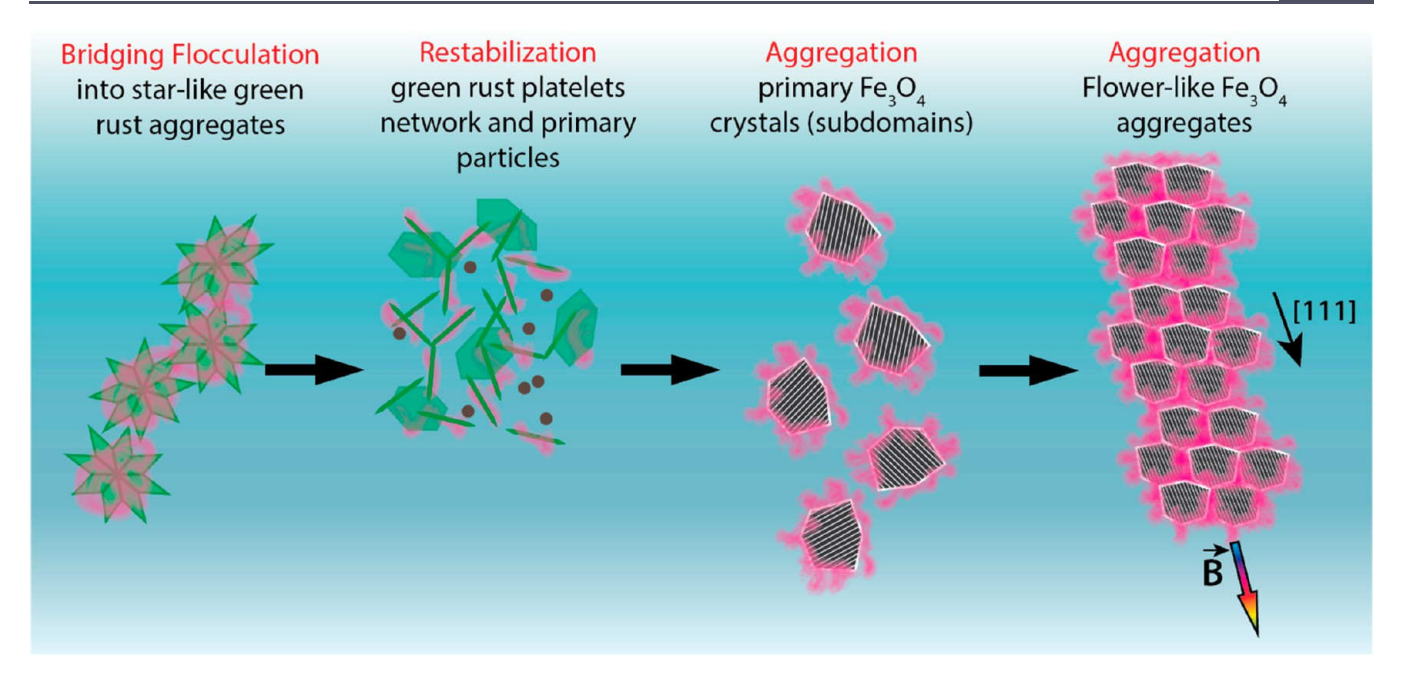


Figure 5. Schematic representation of the proposed steps in the formation of flower-like magnetite aggregates.

nm, the largest, as shown in Figure 4. The magnetic flux density map (Figure 4a) shows the magnetic field distribution and its strength visualized using contour lines and colors. A majority of the crystals form a stable single magnetic domain; however, the magnetic state of large crystals at the end of the chain suggests a complex magnetic state with curling flux lines forming a vortex-like state. Three small ~30 nm crystals on the left side of the chain show no magnetic signal. These crystals are close to the superparamagnetic limit and may not have reversed their magnetization during the reversal. The crystal in the chain marked by "B" that does not overlap with others and has a well-defined single magnetic state has been selected and analyzed in greater detail. Its size is measured as 70 nm using a bright field TEM image (not shown). The magnetic phase shift for a spherical 70 nm Fe₃O₄ crystal with saturation magnetization of 0.6 T is 1.52 rad, 50 which is in good match with the measured phase shift of 1.5 ± 0.2 rad (Figure S7). The same behavior was reported for mesocrystalline magnetite aggregates formed in the presence of polyarginine, 45 in contrast with another study in which magnetite mesocrystals synthesized in the presence of diethylene glycol exhibit a superparamagnetic (SP) behavior. 18,23 Thus, the subunits are crystallographically aligned, and while in the SP regime, they form a stable single magnetic domain, facilitating chain formation. Because the easy magnetization direction for magnetite is along the [111] plane, the magnetism might play a role in the crystallographic alignment of the subdomains. The results show a hierarchical alignment of the magnetite aggregates, crystallographically and magnetically. These alignments can occur sequentially to each other or simultaneously as the SP subdomains possess a certain degree of rotational freedom. However, there are no experimental results that can distinguish between the two mechanisms. The electrostatic potential of the mesocrystals marked by "A" and "B" is also studied using the measured MIP potentials. The size of crystal A was measured on bright field TEM images as 83 nm (crystal B is 70 nm). For spherical particles, assuming a MIP of 17 V and an accelerating voltage of 300 kV, the MIPs at the center of 83 and 70 nm particles relative to its surrounding are predicted to be 9.2 and 7.77 rad,

respectively. These values are larger than the experimentally measured values of 7.9 ± 0.15 and 7 ± 0.15 rad, respectively, suggesting that the Fe₃O₄ mesocrystals have a density that is slightly lower than that of pure magnetite. The discrepancy in the phase shift measurements relative to pure Fe₃O₄ can be explained by the presence of pAA in the gaps of individual units as the electron tomography experiments revealed (Figure 2).

CONCLUSIONS

Here, we present a study of the intermediate stages during the aqueous formation of Fe_3O_4 aggregates in the presence of pAA. The cryo-TEM micrographs (Figure 1 and Supporting Information section 1) reveal that magnetite is formed through a multistep process. First, green rust platelets are formed that transform into \sim 5 nm primary particles (Figure 1b). In a second step, the agglomeration of primary particles, probably through an oriented attachment mechanism, 31,51 forms magnetite crystals in the size range of 10 nm that represent the subunits. Finally, the aggregation of these magnetite subunits produces the final mesocrystalline magnetic structure. Figure 5 shows the schematic of this proposed stepwise growth mechanism summarizing the experimental observations discussed in this study.

The polymer plays a crucial role in this process. In the early stages of the reaction, green rust platelets aggregate (star-like aggregates) due to the electrostatic absorption of pAA on the platelet surfaces according to the bridging flocculation phenomenon. While the green rust is consumed during the formation of magnetite, the colloidal stabilization of the precursor prevails in the flocculation with a consequent decrease in the frequency of the star-like aggregates. At the same time, the polymer is also interacting with the forming magnetite mineral phase. This interaction is due to the fact that some of the magnetite crystalline planes expose Fe that can coordinate with carboxylate groups. In fact, the 3D reconstructed volume visualization (Figure 2d,e) of the crystal structure shows that the cracks, propagating through the structure, are located at approximately 90° to each other,

supporting the idea of a directional absorption of the polymer. Therefore, pAA would not absorb completely on the Fe_3O_4 surface giving rise to the depletion interaction 52 (see Supporting Information section 3) that could contribute to promoting the aggregation of both primary particles and subunits.

3D reconstruction of the mesocrystals shows that the subunits are crystallographically aligned in the Fe_3O_4 aggregates. Interestingly, even though the crystals are composed of subdomains in the SP regime, the overall structure displays magnetic properties depending on the final crystal size (either SSD or MD) as expected for magnetite crystals formed in the absence of any additives. Furthermore, the presence of isolated Fe_3O_4 aggregates at early stages (7 min in Figure 1g) but not in the end product suggests that the magnetism of the crystals also evolves during the reaction.

The magnetic imaging studies reveal that the aggregates arranged in chains present a single stable magnetic domain or a complex state (e.g., vortex) depending on the crystal size. In solution, magnetite aggregates that are not arranged with other magnetite crystals are observed, possibly due to the large size that decreased their diffusion coefficient in solution. Nevertheless, these large isolated aggregates still present a crystallographic alignment (Figures S1 and S4).

This work provides new insights into the formation mechanism of multicore magnetite aggregates that can be useful for designing material for future applications. Controlling the formation step of the subunits or affecting the aggregation step of the magnetite subunit, the shape and magnetic state of the crystals will be helpful for technological applications and/or biomedical applications, such as cancer therapy.

■ MATERIALS AND METHODS

Magnetite Synthesis. Polyacrylic acid (pAA, $M_{\rm w} \sim 450000~{\rm Da}$), FeCl₂·4H₂O, and FeSO₄·7H₂O were purchased from Sigma-Aldrich. KNO₃ and KOH were purchased from Merck. All chemicals were used as received. All solutions were prepared using Milli-Q water (18.2 MΩ, Millipore, 20 °C), which was degassed using either a nitrogen gas flow or an argon gas flow for at least 30 min prior use. A mixture containing 7 mL of 0.5 M KOH, 10 mL of 0.5 M KNO₃, and 0.0456 g of pAA was prepared and degassed. This mixture was then added to a three-neck round-bottom flask containing 8 mL of 0.08 M FeSO₄·7H₂O, and immediately after that, a dark green precipitate was formed, which gradually converted into black magnetite. The entire synthesis was performed under a continuous nitrogen flow at 90 °C, with a final pH value of ~13–14. After 4–6 h, the reaction was stopped and the solution product stored in a vial sealed under nitrogen.

Transmission Electron Microscopy. Cryo-TEM. For cryo-TEM, we used 200 mesh Cu grids with Quantifoil R 2/2 holey carbon films (Quantifoil Micro Tools GmbH). For the cryogenic sample preparation, we used an automated vitrification robot (FEI Vitrobot Mark III) to plunge each sample into liquid ethane in preparation for cryo-TEM.⁵³ Prior to being used, the TEM grids were glow discharged for 40 s with a Cressington 208 carbon coater to render them hydrophilic. Samples were analyzed on the Titan Krios instrument (FEI) operated at 300 kV, equipped with a field emission gun (FEG), a postcolumn Gatan Energy Filter (GIF), and a post-GIF Gatan CCD camera (2048 × 2048 pixels). A Gatan Digital Micrograph (including DiffTools) and MATLAB were used to analyze the TEM image and SAED pattern, respectively. Enlargements of the TEM images were filtered by applying a low path filter to enhance their quality.

Electron Tomography (ET). Tomographic tilt series were acquired from a dry sample at room temperature, and 200 mesh Cu grids with

continuous 2 nm carbon films (Agar Scientific) were used. For the tomographic sample preparation, first a solution containing 5 nm gold nanoparticles (fiducials) was applied and dried with air. Afterward, 50 μ L of the sample solution was applied to the TEM grid and dried with air. Prior to being used, the TEM grids were glow discharged for 40 s by a Cressington 208 carbon coater to render them hydrophilic. Tomographic samples were analyzed on a Titan instrument (FEI, www.cryotem.nl) operated at 300 kV, equipped with a field emission gun (FEG), a postcolumn GIF, and a post-GIF Gatan CCD camera (2048 × 2048 pixels). A Gatan Digital Micrograph (including DiffTools) and MATLAB were used to analyze the TEM image and SAED pattern, respectively. For the acquisition of the tomographic tilt series, a single rotation axis was used to tilt the stage from -68° to 68° in 2° intervals. Focus was determined from the image shift of the gold fiducials, applying beam tilting of 16 mrad between the images. The tomographic tilt series was processed to obtain the reconstruction by using a simultaneous iterative reconstruction technique (SIRT).5

Off-Axis Electron Holography. The samples were prepared on lacey carbon-covered Cu grids by applying $\sim\!50~\mu\text{L}$ of sample solutions and drying in vacuum. The electron holograms were recorded using the spherical-aberration-corrected FEI Titan "Holo" microscope at Ernst Ruska-Centre for Microscopy and Spectroscopy with Electrons in Forschungszentrum Jülich. It was operated under magnetic field free conditions (Lorentz mode) at an acceleration voltage of 300 kV. The holograms were recorded using a conventional CCD camera at 2048 \times 2048 pixels (Gatan Ultrascan) and a Fischione dual-axis tomography holder. Further details regarding the acquisition procedure can be found in Supporting Information section 6.

Crystal Size Measurements. Crystal size distributions were determined by manually measuring the long and short axes of more than 100 individual crystals per sample in TEM images using a MATLAB program. The average of long and short axis for each crystal was taken as the crystal size, and \pm indicates the standard deviation of the mean.

ASSOCIATED CONTENT

Supporting Information

The Supporting Information is available free of charge on the ACS Publications website at DOI: 10.1021/acs.chemmater.9b01836.

Video of the reconstructed tomogram of a typical magnetite aggregate (AVI)

Additional discussion and supplementary figures (PDF) Video of the manual segmentation of the aggregate and the gaps (AVI)

Video of the distance transform map obtained from the distance-based watershed process (AVI)

Video of the final labeled segmentation volume (AVI)

AUTHOR INFORMATION

Corresponding Authors

*E-mail: h.friedrich@tue.nl. *E-mail: n.sommerdijk@tue.nl.

ORCID (

Giulia Mirabello: 0000-0002-8009-3758

Nico A. J. M. Sommerdijk: 0000-0002-8956-195X

Heiner Friedrich: 0000-0003-4582-0064

Present Address

A. Keizer: Orsay Physics (Tescan-Orsay Holding), ZAC Saint-Charles, 3ème rue n°95, F-13710 Fuveau, France.

Author Contributions

N.A.J.M.S., H.F., G.M., and A. Keizer conceived and designed the experiments. A. Keizer and G.M. performed the synthetic

experiments. H.F., P.H.H.B., G.M., and A. Keizer conceived and designed the TEM, ET, and cryo-TEM experiments. A. Keizer, G.M., and P.H.H.B. performed the TEM, ET, and cryo-TEM acquisition. G.M. and A. Keizer performed the cryo-TEM analysis. H.F. and A. Keizer performed the ET analysis. R.E.D.-B. and A. Kovács conceived and designed the EH experiments. A. Kovács, G.M., and A. Keizer performed the EH acquisition. A. Kovács performed the EH analysis. The manuscript was written through contributions of all authors. All authors have given approval to the final version of the manuscript.

Notes

The authors declare no competing financial interest.

ACKNOWLEDGMENTS

G.M. thanks Prof. R. Tuinier for the valuable discussion about the polymer effect. The authors thank Prof. G. de With for critically reading the manuscript and L. S. van Hazendonk for helping with the videos of subdomain segmentation. The work of G.M. is supported by the Technology Foundation STW, the applied science division of The Netherlands Organization for Scientific Research [Nederlandse Organizatie voor Wetenschappelijk onderzoek (NWO)].

REFERENCES

- (1) Rosen, J. E.; Chan, L.; Shieh, D.-B.; Gu, F. X. Iron oxide nanoparticles for targeted cancer imaging and diagnostics. *Nanomedicine* **2012**, *8* (3), 275–290.
- (2) Cabrera, D.; Coene, A.; Leliaert, J.; Artés-Ibáñez, E. J.; Dupré, L.; Telling, N. D.; Teran, F. J. Dynamical Magnetic Response of Iron Oxide Nanoparticles Inside Live Cells. *ACS Nano* **2018**, *12* (3), 2741–2752.
- (3) Revia, R. A.; Zhang, M. Magnetite nanoparticles for cancer diagnosis, treatment, and treatment monitoring: recent advances. *Mater. Today* **2016**, *19* (3), 157–168.
- (4) Stephen, Z. R.; Kievit, F. M.; Zhang, M. Magnetite nanoparticles for medical MR imaging. *Mater. Today* **2011**, *14* (7), 330–338.
- (5) Wu, M.; Huang, S. Magnetic nanoparticles in cancer diagnosis, drug delivery and treatment. *Mol. Clin. Oncol.* **2017**, *7* (5), 738–746.
- (6) Wani, K. D.; Kadu, B. S.; Mansara, P.; Gupta, P.; Deore, A. V.; Chikate, R. C.; Poddar, P.; Dhole, S. D.; Kaul-Ghanekar, R. Synthesis, Characterization and In Vitro Study of Biocompatible Cinnamaldehyde Functionalized Magnetite Nanoparticles (CPGF Nps) For Hyperthermia and Drug Delivery Applications in Breast Cancer. *PLoS One* **2014**, *9* (9), No. e107315.
- (7) Mondal, S.; Manivasagan, P.; Bharathiraja, S.; SanthaMoorthy, M.; Nguyen, V.; Kim, H.; Nam, S.; Lee, K.; Oh, J. Hydroxyapatite Coated Iron Oxide Nanoparticles: A Promising Nanomaterial for Magnetic Hyperthermia Cancer Treatment. *Nanomaterials* **2017**, 7 (12), 426.
- (8) Dabbagh, A.; Hedayatnasab, Z.; Karimian, H.; Sarraf, M.; Yeong, C. H.; Madaah Hosseini, H. R.; Abu Kasim, N. H.; Wong, T. W.; Rahman, N. A. Polyethylene glycol-coated porous magnetic nanoparticles for targeted delivery of chemotherapeutics under magnetic hyperthermia condition. *Int. J. Hyperthermia* **2019**, *36* (1), 104–114.
- (9) Moroz, P.; Jones, S. K.; Gray, B. N. Magnetically mediated hyperthermia: current status and future directions. *Int. J. Hyperthermia* **2002**, *18* (4), 267–284.
- (10) Fairbairn, J. J.; Khan, M. W.; Ward, K. J.; Loveridge, B. W.; Fairbairn, D. W.; O'Neill, K. L. Induction of apoptotic cell DNA fragmentation in human cells after treatment with hyperthermia. *Cancer Lett.* **1995**, 89 (2), 183–188.
- (11) Ahmed, K.; Tabuchi, Y.; Kondo, T. Hyperthermia: an effective strategy to induce apoptosis in cancer cells. *Apoptosis* **2015**, *20* (11), 1411–1419.

(12) Li, T.-J.; Huang, C.-C.; Ruan, P.-W.; Chuang, K.-Y.; Huang, K.-J.; Shieh, D.-B.; Yeh, C.-S. In vivo anti-cancer efficacy of magnetite nanocrystal - based system using locoregional hyperthermia combined with 5-fluorouracil chemotherapy. *Biomaterials* **2013**, *34* (32), 7873–7883

- (13) Kawai, N.; Ito, A.; Nakahara, Y.; Honda, H.; Kobayashi, T.; Futakuchi, M.; Shirai, T.; Tozawa, K.; Kohri, K. Complete regression of experimental prostate cancer in nude mice by repeated hyperthermia using magnetite cationic liposomes and a newly developed solenoid containing a ferrite core. *Prostate* **2006**, *66* (7), 718–727.
- (14) Venditto, V. J.; Szoka, F. C. Cancer nanomedicines: So many papers and so few drugs! Adv. Drug Delivery Rev. 2013, 65 (1), 80–88.
- (15) Wicki, A.; Witzigmann, D.; Balasubramanian, V.; Huwyler, J. Nanomedicine in cancer therapy: Challenges, opportunities, and clinical applications. *J. Controlled Release* **2015**, *200*, 138–157.
- (16) Park, K. Facing the Truth about Nanotechnology in Drug Delivery. ACS Nano 2013, 7 (9), 7442–7447.
- (17) Mahmoudi, K.; Bouras, A.; Bozec, D.; Ivkov, R.; Hadjipanayis, C. Magnetic hyperthermia therapy for the treatment of glioblastoma: a review of the therapy's history, efficacy and application in humans. *Int. J. Hyperthermia* **2018**, 34, 1316–1328.
- (18) Hugounenq, P.; Levy, M.; Alloyeau, D.; Lartigue, L.; Dubois, E.; Cabuil, V.; Ricolleau, C.; Roux, S.; Wilhelm, C.; Gazeau, F.; Bazzi, R. Iron Oxide Monocrystalline Nanoflowers for Highly Efficient Magnetic Hyperthermia. *J. Phys. Chem. C* **2012**, *116* (29), 15702–15712.
- (19) Schaller, V.; Wahnström, G.; Sanz-Velasco, A.; Gustafsson, S.; Olsson, E.; Enoksson, P.; Johansson, C. Effective magnetic moment of magnetic multicore nanoparticles. *Phys. Rev. B: Condens. Matter Mater. Phys.* **2009**, *80* (9), 092406.
- (20) Rosensweig, R. E. Heating magnetic fluid with alternating magnetic field. J. Magn. Magn. Mater. 2002, 252, 370-374.
- (21) Kafrouni, L.; Savadogo, O. Recent progress on magnetic nanoparticles for magnetic hyperthermia. *Progress in Biomaterials* **2016**, *5*, 147–160.
- (22) Thomas, L. A.; Dekker, L.; Kallumadil, M.; Southern, P.; Wilson, M.; Nair, S. P.; Pankhurst, Q. A.; Parkin, I. P. Carboxylic acid-stabilised iron oxide nanoparticles for use in magnetic hyperthermia. *J. Mater. Chem.* **2009**, *19* (36), 6529–6535.
- (23) Lartigue, L.; Hugounenq, P.; Alloyeau, D.; Clarke, S. P.; Lévy, M.; Bacri, J.-C.; Bazzi, R.; Brougham, D. F.; Wilhelm, C.; Gazeau, F. Cooperative Organization in Iron Oxide Multi-Core Nanoparticles Potentiates Their Efficiency as Heating Mediators and MRI Contrast Agents. ACS Nano 2012, 6 (12), 10935–10949.
- (24) Cao, S.-W.; Zhu, Y.-J.; Chang, J. Fe3O4 polyhedral nanoparticles with a high magnetization synthesized in mixed solvent ethylene glycol-water system. *New J. Chem.* **2008**, 32 (9), 1526–1530.
- (25) Wan, J.; Tang, J.; Zhang, C.; Yuan, R.; Chen, K. Insight into the formation of magnetite mesocrystals from ferrous precursors in ethylene glycol. *Chem. Commun.* **2015**, *51* (88), 15910–15913.
- (26) Ge, J.; Hu, Y.; Biasini, M.; Beyermann, W. P.; Yin, Y. Superparamagnetic Magnetite Colloidal Nanocrystal Clusters. *Angew. Chem., Int. Ed.* **2007**, 46 (23), 4342–4345.
- (27) Altan, C. L.; Gurten, B.; Sadza, R.; Yenigul, E.; Sommerdijk, N. A. J. M.; Bucak, S. Poly(acrylic acid)-directed synthesis of colloidally stable single domain magnetite nanoparticles via partial oxidation. *J. Magn. Magn. Mater.* **2016**, *416*, 366–372.
- (28) Sturm, E. V.; Colfen, H. Mesocrystals: structural and morphogenetic aspects. *Chem. Soc. Rev.* **2016**, 45 (21), 5821–5833.
- (29) Brunner, J.; Baburin, I. A.; Sturm, S.; Kvashnina, K.; Rossberg, A.; Pietsch, T.; Andreev, S.; Sturm, E.; Cölfen, H. Self-Assembled Magnetite Mesocrystalline Films: Toward Structural Evolution from 2D to 3D Superlattices. *Adv. Mater. Interfaces* **2017**, *4* (1), 1600431.
- (30) Sturm, E.; Cölfen, H. Mesocrystals: Past, Presence, Future. Crystals 2017, 7 (7), 207.
- (31) Baumgartner, J.; Dey, A.; Bomans, P. H. H.; Le Coadou, C.; Fratzl, P.; Sommerdijk, N. A. J. M.; Faivre, D. Nucleation and growth of magnetite from solution. *Nat. Mater.* **2013**, *12* (4), 310–314.

(32) Deegan, R. D.; Bakajin, O.; Dupont, T. F.; Huber, G.; Nagel, S. R.; Witten, T. A. Capillary flow as the cause of ring stains from dried liquid drops. *Nature* **1997**, *389*, 827.

- (33) Patterson, J. P.; Xu, Y.; Moradi, M.-A.; Sommerdijk, N. A. J. M.; Friedrich, H. CryoTEM as an Advanced Analytical Tool for Materials Chemists. *Acc. Chem. Res.* **2017**, *50* (7), 1495–1501.
- (34) Sugimoto, T.; Matijević, E. Formation of Uniform Spherical Magnetite Particles by Crystallization from Ferrous Hydroxide Gels. *J. Colloid Interface Sci.* **1980**, 74 (1), 227–243.
- (35) Altan, C. L.; Lenders, J. J. M.; Bomans, P. H. H.; de With, G.; Friedrich, H.; Bucak, S.; Sommerdijk, N. A. J. M. Partial Oxidation as a Rational Approach to Kinetic Control in Bioinspired Magnetite Synthesis. *Chem. Eur. J.* **2015**, 21 (16), 6150–6156.
- (36) Trolard, F.; Bourrié, G. Structure of fougerite and green rusts and a thermodynamic model for their stabilities. *J. Geochem. Explor.* **2006**, 88 (1), 249–251.
- (37) Mirabello, G.; Lenders, J. J. M.; Sommerdijk, N. A. J. M. Bioinspired synthesis of magnetite nanoparticles. *Chem. Soc. Rev.* **2016**, 45 (18), 5085–5106.
- (38) Vereda, F.; de Vicente, J.; Hidalgo-Alvarez, R. Oxidation of ferrous hydroxides with nitrate: A versatile method for the preparation of magnetic colloidal particles. *J. Colloid Interface Sci.* **2013**, 392, 50–56
- (39) Mączka, E.; Jartych, E.; Kosmulski, M. Isoelectric points of fresh and aged Fe(OH)2. *Colloids Surf., A* **2014**, 441, 326–330.
- (40) Erdemoğlu, M.; Sarıkaya, M. Effects of heavy metals and oxalate on the zeta potential of magnetite. *J. Colloid Interface Sci.* **2006**, 300 (2), 795–804.
- (41) Cornell, R. M.; Schwertmann, U. Surface Chemistry and Colloidal Stability. In *The Iron Oxides: Structure, Properties, Reactions, Occurences and Uses*; Wiley, 2003.
- (42) Staniland, S. S.; Rawlings, A. E. Crystallizing the function of the magnetosome membrane mineralization protein Mms6. *Biochem. Soc. Trans.* **2016**, 44 (3), 883–890.
- (43) Cornell, R. M.; Schwertmann, U. The iron oxides: structure, properties, reactions, occurrences and uses; John Wiley & Sons, 2006.
- (44) Pelssers, E. G. M.; Stuart, M. A. C.; Fleer, G. J. Kinetics of bridging flocculation. Role of relaxations in the polymer layer. *J. Chem. Soc., Faraday Trans.* **1990**, 86 (9), 1355–1361.
- (45) Reichel, V.; Kovács, A.; Kumari, M.; Bereczk-Tompa, É.; Schneck, E.; Diehle, P.; Pósfai, M.; Hirt, A. M.; Duchamp, M.; Dunin-Borkowski, R. E.; Faivre, D. Single crystalline superstructured stable single domain magnetite nanoparticles. *Sci. Rep.* **2017**, *7*, 45484.
- (46) Wade, R. H. A brief look at imaging and contrast transfer. *Ultramicroscopy* **1992**, *46* (1), 145–156.
- (47) Dunlop, D. J.; Özdemir, Ö. Rock Magnetism: Fundamentals and Frontiers; Cambridge University Press: Cambridge, U.K., 1997.
- (48) Midgley, P. A.; Dunin-Borkowski, R. E. Electron tomography and holography in materials science. *Nat. Mater.* **2009**, *8*, 271.
- (49) Thomas, J. M.; Simpson, E. T.; Kasama, T.; Dunin-Borkowski, R. E. Electron Holography for the Study of Magnetic Nanomaterials. *Acc. Chem. Res.* **2008**, *41* (5), 665–674.
- (50) Kasama, T.; Dunin-Borkowski, R. E.; Beleggia, M. Electron holography of magnetic materials. In *Holography-Different Fields of Application*; Ramirez, F. A. M., Ed.; InTech, 2011; pp 53–80.
- (51) Li, D.; Nielsen, M. H.; Lee, J. R. I.; Frandsen, C.; Banfield, J. F.; De Yoreo, J. J. Direction-Specific Interactions Control Crystal Growth by Oriented Attachment. *Science* **2012**, *336* (6084), 1014–1018.
- (52) Lekkerkerker, H. N. W.; Tuinier, R. Colloids and the Depletion Interaction; Springer: Dordrecht, The Netherlands, 2011; Vol. 833.
- (53) Vos, M. R.; Bomans, P. H. H.; Frederik, P. M.; Sommerdijk, N. A. J. M. The development of a glove-box/Vitrobot combination: Airwater interface events visualized by cryo-TEM. *Ultramicroscopy* **2008**, *108* (11), 1478–1483.
- (54) Chen, D.; Goris, B.; Bleichrodt, F.; Mezerji, H. H.; Bals, S.; Batenburg, K. J.; de With, G.; Friedrich, H. The properties of SIRT, TVM, and DART for 3D imaging of tubular domains in nanocomposite thin-films and sections. *Ultramicroscopy* **2014**, *147*, 137–148.